Astronomy & Astrophysics manuscript no. paper
December 20, 2012

© ESO 2012

arXiv:1212.4077v2 [astro-ph.SR] 19 Dec 2012

Competition of rotation and stratification in flux concentrations

I. R. Losada[1,2,3,4], A. Brandenburg[3,4], N. Kleeorin[5,3], I. Rogachevskii[5,3]

[1] Department of Astrophysics, Universidad de La Laguna, 38206 La Laguna (Tenerife), Spain
[2] Instituto de Astrofísica de Canarias, C/ Vía Láctea, s/n, La Laguna, Tenerife, Spain
[3] Nordita, KTH Royal Institute of Technology and Stockholm University, Roslagstullsbacken 23, 10691 Stockholm, Sweden
[4] Department of Astronomy, AlbaNova University Center, Stockholm University, 10691 Stockholm, Sweden
[5] Department of Mechanical Engineering, Ben-Gurion University of the Negev, POB 653, Beer-Sheva 84105, Israel

December 20, 2012, Revision: 1.54

ABSTRACT

Context. In a strongly stratified turbulent layer, a uniform horizontal magnetic field can become unstable to form spontaneously local flux concentrations due to a negative contribution of turbulence to the large-scale (mean-field) magnetic pressure. This mechanism is of interest in connection with dynamo scenarios in which most of the magnetic field resides in the bulk of the convection zone, and not at the bottom, as is usually assumed. Recent work using the mean-field hydromagnetic equations has shown that this negative effective magnetic pressure instability (NEMPI) becomes suppressed at rather low rotation rates with Coriolis numbers as low as 0.1.
Aims. Here we extend these earlier investigations by studying the effects of rotation both on the development of NEMPI and on the effective magnetic pressure (turbulent and non-turbulent contributions). We quantify the kinetic helicity resulting from rotation and stratification and compare with earlier work at smaller scale-separation ratios. We also determine the sensitivity of surface diagnostics of magnetic helicity.
Methods. We use direct numerical simulations (DNS) and mean-field calculations of the three-dimensional hydromagnetic equations in a Cartesian domain and analytical studies using the τ approach.
Results. We find that the growth rates of NEMPI in earlier mean-field calculations are well reproduced with DNS and that the rotational effect on the effective magnetic pressure is negligible as long as the production of flux concentrations is not inhibited by rotation. In that case, kinetic and magnetic helicity are also found to be weak.
Conclusions. Production of magnetic flux concentrations through the suppression of turbulent pressure appears to be possible only in the upper-most layers of the Sun, where the convective turnover time is less than 2 hours.

Key words. magnetohydrodynamics (MHD) – hydrodynamics – turbulence – Sun: dynamo

1. Introduction

In the Sun, magnetic fields are produced by a large-scale dynamo (see, e.g., Moffatt, 1978; Parker, 1979; Krause & Rädler, 1980; Zeldovich et al., 1983; Ossendrijver, 2003; Brandenburg & Subramanian, 2005a). Although many details of this process remain subject to debate, it seems relatively clear that rotation enhances the efficiency of the dynamo if the Coriolis parameter is not very large. In the absence of rotation and shear, only small-scale magnetic fields are generated by what is often referred to as small-scale dynamo action (see, e.g., Zeldovich et al., 1990; Brandenburg & Subramanian, 2005a). Rotation leads to an α effect (Steenbeck et al., 1966) if there is also stratification in density or turbulent intensity. The α effect can produce mean magnetic field and net magnetic flux.

Stratification leads to yet another effect which does not produce magnetic flux, but merely concentrates it locally by what is now referred to as negative effective magnetic pressure instability (NEMPI). Direct numerical simulations (DNS) of Brandenburg et al. (2011a) have shown in surprising detail many aspects of NEMPI that were previously seen in mean-field simulations (MFS) of Brandenburg et al. (2010) and that have been anticipated based on analytical studies for some time (Kleeorin et al., 1989, 1990, 1993, 1996; Kleeorin & Rogachevskii, 1994; Rogachevskii & Kleeorin, 2007).

The main physics of this effect is connected with the suppression of turbulent pressure by a weak mean magnetic field that is less than the equipartition field. At large Reynolds numbers, the resulting reduction of the turbulent pressure is larger than the added magnetic pressure from the mean magnetic field itself, so that the *effective* magnetic pressure that accounts for turbulent and non-turbulent contributions, becomes negative. In a strongly stratified layer, i.e., a layer in which the density varies much more rapidly with height than the magnetic field, this leads to an instability that is analogous to Parker's magnetic buoyancy instability, except that there the magnetic field varies more rapidly with height than the density. Because the effective magnetic pressure is negative, magnetic structures are negatively buoyant and sink, which has been seen in DNS of Brandenburg et al. (2011a).

One of the main successes of recent comparative work between DNS and MFS is the demonstration of a high degree of predictive power of MFS. The examples include details regarding the shape and evolution of structures, the dependence of their depth on the magnetic field strength, and the dependence of the growth rate on the scale separation ratio. Recent MFS of Losada et al. (2012) (hereafter LBKMR) have shown that in the presence of even just weak rotation, the growth rate of NEMPI is significantly reduced. Expressed in terms of the Coriolis number, Co $= 2\Omega/u_{\rm rms}k_{\rm f}$, where Ω is the angular velocity, $u_{\rm rms}$ is the rms velocity of the turbulence, and $k_{\rm f}$ is the wavenumber of the energy-carrying eddies, the critical value of Co was predicted to be as low as 0.03. Although this value does not preclude the operation of NEMPI in the upper parts of the Sun, where Co is indeed small (about 10^{-4} at the surface), it does seem surprisingly low, which raises questions regarding the accuracy of MFS in this case. The purpose of the present paper is therefore to compare MFS of LBKMR with DNS of the same setup.

The MFS of LBKMR were done for a case for which comparisons between MFS and DNS do exist in the special case of $\mathrm{Co}=0$ (Kemel et al., 2012a). The aim of this paper is to extend these effects to the case of non-vanishing values of the Coriolis number Co. We use DNS of the MHD equations and analytical studies based on the τ approach. We recall that we adopt here an isothermal stratification and an isothermal equation of state. This is done because the effect that we are interested in exists even in this simplest case where temperature and pressure scale height are constant. Non-isothermal setups have been studied at the mean-field level both with (Käpylä et al., 2012, 2013) and without (Brandenburg et al., 2010) entropy evolution included. In a stably stratified layer, entropy evolution leads to an additional restoring force and hence to internal gravity waves (Brunt-Väisälä oscillations) that stabilize NEMPI (Käpylä et al., 2012). Thus, by using both isothermal stratification and an isothermal equation of state, we recover a situation that is similar to an adiabatic layer, except that then the temperature and hence the pressure scale height decrease with height.

2. The model

We consider DNS of an isothermally stratified layer (Brandenburg et al., 2011a; Kemel et al., 2012a) and solve the equations for the velocity $\boldsymbol{U}$, the magnetic vector potential $\boldsymbol{A}$, and the density ρ, in the presence of rotation Ω,

$$\frac{\mathrm{D}\boldsymbol{U}}{\mathrm{D}t} = -2\boldsymbol{\Omega}\times\boldsymbol{U} - c_\mathrm{s}^2\boldsymbol{\nabla}\ln\rho + \frac{1}{\rho}\boldsymbol{J}\times\boldsymbol{B} + \boldsymbol{f} + \boldsymbol{g} + \boldsymbol{F}_\nu, \quad (1)$$

$$\frac{\partial\boldsymbol{A}}{\partial t} = \boldsymbol{U}\times\boldsymbol{B} + \eta\nabla^2\boldsymbol{A}, \quad (2)$$

$$\frac{\partial\rho}{\partial t} = -\boldsymbol{\nabla}\cdot\rho\boldsymbol{U}, \quad (3)$$

where $\mathrm{D}/\mathrm{D}t = \partial/\partial t + \boldsymbol{U}\cdot\boldsymbol{\nabla}$ is the advective derivative, ν is the kinematic viscosity, η is the magnetic diffusivity due to Spitzer conductivity of the plasma, $\boldsymbol{B} = \boldsymbol{B}_0 + \boldsymbol{\nabla}\times\boldsymbol{A}$ is the magnetic field, $\boldsymbol{B}_0 = (0, B_0, 0)$ is the imposed uniform field, $\boldsymbol{J} = \boldsymbol{\nabla}\times\boldsymbol{B}/\mu_0$ is the current density, μ_0 is the vacuum permeability, $\boldsymbol{F}_\nu = \boldsymbol{\nabla}\cdot(2\nu\rho\boldsymbol{\mathsf{S}})$ is the viscous force, $\mathsf{S}_{ij} = \frac{1}{2}(\partial_j U_i + \partial_i U_j) - \frac{1}{3}\delta_{ij}\boldsymbol{\nabla}\cdot\boldsymbol{U}$ is the traceless rate-of-strain tensor. The angular velocity vector $\boldsymbol{\Omega}$ is quantified by its scalar amplitude Ω and colatitude θ, such that $\boldsymbol{\Omega} = \Omega\,(-\sin\theta, 0, \cos\theta)$. As in LBKMR, z corresponds to radius, x to colatitude, and y to azimuth. The forcing function $\boldsymbol{f}$ consists of random, white-in-time, plane, non-polarized waves with a certain average wavenumber k_f. The turbulent rms velocity is approximately independent of z with $u_\mathrm{rms} = \langle\boldsymbol{u}^2\rangle^{1/2} \approx 0.1\,c_\mathrm{s}$. The gravitational acceleration $\boldsymbol{g} = (0, 0, -g)$ is chosen such that $k_1 H_\rho = 1$, so the density contrast between bottom and top is $\exp(2\pi) \approx 535$ in a domain $-\pi \le k_1 z \le \pi$. Here, $H_\rho = c_\mathrm{s}^2/g$ is the density scale height and $k_1 = 2\pi/L$ is the smallest wavenumber that fits into the cubic domain of size L^3. In most of our calculations, structures develop whose horizontal wavenumber k_x is close to k_1. We adopt Cartesian coordinates (x, y, z), with periodic boundary conditions in the x- and y-directions and stress-free, perfectly conducting boundaries at the top and bottom ($z = \pm L_z/2$). In all cases, we use a scale separation ratio k_f/k_1 of 30, a fluid Reynolds number $\mathrm{Re} \equiv u_\mathrm{rms}/\nu k_\mathrm{f}$ of 36, and a magnetic Prandtl number $\mathrm{Pr}_M = \nu/\eta$ of 0.5. The magnetic Reynolds number is therefore $\mathrm{Re}_M = \mathrm{Pr}_M\mathrm{Re} = 18$. The value of B_0 is specified in units of the volume-averaged value $B_\mathrm{eq0} = \sqrt{\mu_0\rho_0}\,u_\mathrm{rms}$, where $\rho_0 = \langle\rho\rangle$ is the volume-averaged density, which is constant in time. In our units, $k_1 = c_\mathrm{s} = \mu_0 = \rho_0 = 1$. In addition to visualizations of the actual magnetic field, we also monitor $\overline{B}_y$, which is an average over y and a certain time interval Δt. Time is sometimes specified in terms of turbulent-diffusive times $t\,\eta_\mathrm{t0}k_1^2$, where $\eta_\mathrm{t0} = u_\mathrm{rms}/3k_\mathrm{f}$ is the estimated turbulent diffusivity.

The simulations are performed with the PENCIL CODE `http://pencil-code.googlecode.com` which uses sixth-order explicit finite differences in space and a third-order accurate time stepping method. We use a numerical resolution of 256^3 mesh points.

We compare with and extend earlier MFS of LBKMR, where we solve the evolution equations for mean velocity $\overline{\boldsymbol{U}}$, mean density $\overline{\rho}$, and mean vector potential $\overline{\boldsymbol{A}}$, in the form

$$\frac{\partial\overline{\boldsymbol{U}}}{\partial t} = -\overline{\boldsymbol{U}}\cdot\boldsymbol{\nabla}\overline{\boldsymbol{U}} - 2\boldsymbol{\Omega}\times\overline{\boldsymbol{U}} - c_\mathrm{s}^2\boldsymbol{\nabla}\ln\overline{\rho} + \boldsymbol{g} + \overline{\boldsymbol{\mathcal{F}}}_\mathrm{MK}, \quad (4)$$

$$\frac{\partial\overline{\boldsymbol{A}}}{\partial t} = \overline{\boldsymbol{U}}\times\overline{\boldsymbol{B}} - (\eta_\mathrm{t} + \eta)\overline{\boldsymbol{J}}, \quad (5)$$

$$\frac{\partial\overline{\rho}}{\partial t} = -\overline{\boldsymbol{U}}\cdot\boldsymbol{\nabla}\overline{\rho} - \overline{\rho}\boldsymbol{\nabla}\cdot\overline{\boldsymbol{U}}, \quad (6)$$

where $\overline{\boldsymbol{\mathcal{F}}}_\mathrm{MK} = \overline{\boldsymbol{\mathcal{F}}}_\mathrm{M} + \overline{\boldsymbol{\mathcal{F}}}_\mathrm{K}$, with

$$\overline{\rho}\,\overline{\boldsymbol{\mathcal{F}}}_\mathrm{M} = -\tfrac{1}{2}\boldsymbol{\nabla}[(1 - q_\mathrm{p})\overline{\boldsymbol{B}}^2] \quad (7)$$

being the mean-field magnetic pressure force, and

$$\overline{\boldsymbol{\mathcal{F}}}_\mathrm{K} = (\nu_\mathrm{t} + \nu)\left(\nabla^2\overline{\boldsymbol{U}} + \tfrac{1}{3}\boldsymbol{\nabla}\boldsymbol{\nabla}\cdot\overline{\boldsymbol{U}} + 2\overline{\boldsymbol{\mathsf{S}}}\boldsymbol{\nabla}\ln\overline{\rho}\right) \quad (8)$$

is the total (turbulent plus microscopic) viscous force. Here, $\overline{\mathsf{S}}_{ij} = \frac{1}{2}(\overline{U}_{i,j} + \overline{U}_{j,i}) - \frac{1}{3}\delta_{ij}\boldsymbol{\nabla}\cdot\overline{\boldsymbol{U}}$ is the traceless rate-of-strain tensor of the mean flow and q_p is approximated by (Kemel et al., 2012b)

$$q_\mathrm{p}(\beta) = \frac{\beta_\star^2}{\beta_\mathrm{p}^2 + \beta^2}, \quad (9)$$

which is only a function of the ratio $\beta \equiv |\overline{\boldsymbol{B}}|/B_\mathrm{eq}$. Here, $\beta_\star$ and β_p are coefficients that have been determined from previous numerical simulations in the absence of rotation (Brandenburg et al., 2012a). In Eq. (7) we have taken into account that the mean magnetic field is independent of y, so the mean magnetic tension vanishes.

The strength of gravitational stratification is characterized by the nondimensional parameter $\mathrm{Gr} = g/c_\mathrm{s}^2k_\mathrm{f} \equiv (H_\rho k_\mathrm{f})^{-1}$ (Brandenburg et al., 2012b). Another important nondimensional parameter is the Coriolis number, $\mathrm{Co} = 2\Omega/u_\mathrm{rms}k_\mathrm{f}$. Alternatively, we normalize the growth rate of the instability by a quantity

$$\lambda_{*0} \equiv \beta_\star u_\mathrm{rms}/H_\rho, \quad (10)$$

which is motivated by the analytic results of LBKMR and the finding that NEMPI is suppressed when $2\Omega \gtrsim \lambda_{*0}$.

3. Coriolis effects of NEMPI in DNS

We have performed DNS for different values of Co and calculated the growth rate λ; see Fig. 1, where we compare with the MFS of LBKMR, who used $q_\mathrm{p0} = 20$ and $\beta_\mathrm{p} = 0.167$. This set of parameters is based on a fit by (Kemel et al., 2012a) for

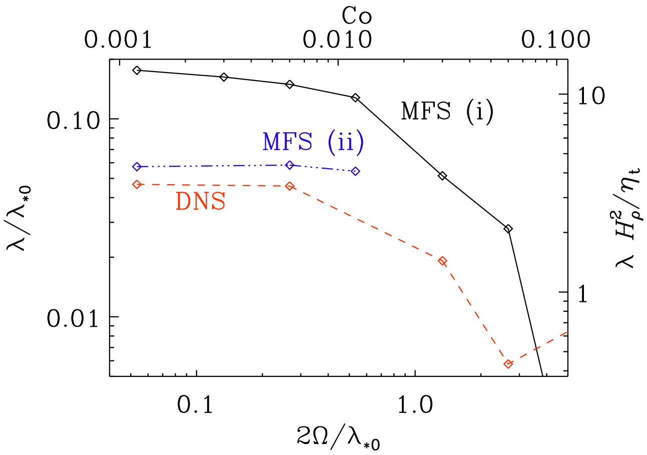

Fig. 1. Dependence of λ/λ_{*0} on $2\Omega/\lambda_{*0}$ for DNS, compared with MFS (i) where $q_{\rm p0}=20$ and $\beta_{\rm p}=0.167$ and MFS (ii) where $q_{\rm p0}=32$ and $\beta_{\rm p}=0.058$. In this case no growth was found for $\mathrm{Co}\geq 0.03$. In all cases we have $B_0/B_{\rm eq0}=0.05$.

$k_{\rm f}/k_1=30$. Note that the growth rates for the MFS are about 3 times larger than those of the DNS; see Appendix A for a revised comparison of the 2-D and 3-D data of LBKMR. This might be caused by an inaccurate estimate of the mean-field coefficients. Indeed, according to Brandenburg et al. (2012a), these parameters should be $q_{\rm p0}=32$ and $\beta_{\rm p}=0.058$ for $\mathrm{Re}_M=18$. We have now performed new 3-D MFS with this set of parameters. Those results are also shown in Fig. 1. It turns out that with these new parameters the resulting growth rates are indeed much closer to those of the DNS, suggesting that the former set of mean-field coefficients might indeed have been inaccurate. A reason for this might be the fact that for $k_{\rm f}/k_1=30$ NEMPI is very strong and leads to inhomogeneous magnetic fields for which the usual determination of mean-field coefficients, as used by Brandenburg et al. (2012a), is no longer valid.

In Fig. 2 we show the yt-averaged $\overline{B}_y$ for $\mathrm{Co}=0.006$, 0.03, and 0.06 at different times. These figures show the generation of structures that begin to sink subsequently. However, for $\mathrm{Co}=0.03$ and larger, this sinking is much less prominent. Instead, the structures remain confined to the surface layers, which is seen more clearly in visualizations of B_y at the periphery of the computational domain for $\mathrm{Co}=0.03$; see Fig. 3.

To our surprise, the large-scale structures remain still independent of the y-direction, which is clearly at variance with results of the corresponding MFS. Even at other angles such as $\theta=45^\circ$ and 90°, no variation in the y-direction is seen; see Fig. 4. The reason for this discrepancy with the corresponding MFS is not yet understood.

4. Effective magnetic pressure

In this section we study the effect of rotation on the function $q_{\rm p}(\beta)$. We consider first the results of DNS and turn then to an analytical treatment.

4.1. Numerical results

In the MFS of LBKMR we assumed that $\mathcal{P}_{\rm eff}(\beta)$ does not change significantly with Co in the range considered. With DNS we can compute $\mathcal{P}_{\rm eff}(\beta)$ by calculating the combined Reynolds and Maxwell stress for a run with and one without an imposed magnetic field. This allows us to compute $q_{\rm p}(\beta)$ using Eq. (17) of Brandenburg et al. (2012a):

$$q_{\rm p}=-2\left[\overline{\rho}\,(\overline{u_x^2}-\overline{u_{0x}^2})+\tfrac{1}{2}\overline{\boldsymbol{b}^2}-\overline{b_x^2}\right]\Big/\overline{\boldsymbol{B}}^2, \tag{11}$$

where the subscripts 0 indicate values obtained from a reference run with $B_0=0$. This expression does not take into account small-scale dynamo action which can produce finite background magnetic fluctuations $\boldsymbol{b}_0$. The effective magnetic pressure is then determined using the equation $\mathcal{P}_{\rm eff}(\beta)=\frac{1}{2}[1-q_{\rm p}(\beta)]$. The result is plotted in Fig. 5 for three values of Co during an early time interval when structure formation is still weak enough so as not to affect the result. We also show the results using Eq. (9) for different combinations of $\beta_\star$ and $\beta_{\rm p}$. It turns out that the curves for $\mathrm{Co}=0$ and 0.03 are close together, and that for $\mathrm{Co}=0.13$ the negative pressure effect is perhaps even slightly enhanced. In any case, it is clear that within the range of values of Co considered, the effect of rotation on $q_{\rm p}$ is quite small.

4.2. Theoretical predictions

Let us now compare with theoretical predictions for $q_{\rm p}(\beta)$. We take into account the feedback of the magnetic field on the turbulent fluid flow. We use a mean-field approach whereby velocity, pressure and magnetic field are separated into mean and fluctuating parts. We also assume vanishing mean motion. The strategy of our analytic derivation is to determine the Ω dependencies of the second moments for the velocity $\overline{u_i(t,\boldsymbol{x})\,u_j(t,\boldsymbol{x})}$, the magnetic field $\overline{b_i(t,\boldsymbol{x})\,b_j(t,\boldsymbol{x})}$, and the cross-helicity tensor $\overline{b_i(t,\boldsymbol{x})\,u_j(t,\boldsymbol{x})}$, where $\boldsymbol{b}$ are fluctuations of magnetic field produced by tangling of the large-scale field. To this end we use the equations for fluctuations of velocity and magnetic field in rotating turbulence, which are obtained by subtracting equations for the mean fields from the corresponding equations for the actual (mean plus fluctuating) fields.

4.2.1. Governing equations

The equations for the fluctuations of velocity and magnetic fields are given by

$$\begin{aligned}\frac{\partial\boldsymbol{u}(\boldsymbol{x},t)}{\partial t} &= -\frac{\boldsymbol{\nabla}p}{\overline{\rho}}+\frac{1}{\overline{\rho}}\left[(\boldsymbol{b}\cdot\boldsymbol{\nabla})\overline{\boldsymbol{B}}+(\overline{\boldsymbol{B}}\cdot\boldsymbol{\nabla})\boldsymbol{b}\right]+2\boldsymbol{u}\times\boldsymbol{\Omega}\\ &\quad+\hat{\mathcal{N}}^u\,, \qquad (12)\\ \frac{\partial\boldsymbol{b}(\boldsymbol{x},t)}{\partial t} &= (\overline{\boldsymbol{B}}\cdot\boldsymbol{\nabla})\boldsymbol{u}-(\boldsymbol{u}\cdot\boldsymbol{\nabla})\overline{\boldsymbol{B}}+\hat{\mathcal{N}}^b\,, \qquad (13)\end{aligned}$$

where Eq. (12) is written in a reference frame rotating with constant angular velocity $\boldsymbol{\Omega}$, $p=p'+(\overline{\boldsymbol{B}}\cdot\boldsymbol{b})$ are the fluctuations of total pressure, p' are the fluctuations of fluid pressure, $\overline{\boldsymbol{B}}$ is the mean magnetic field, and $\overline{\rho}$ is the mean fluid density. For simplicity we neglect effects of compressibility. The terms $\hat{\mathcal{N}}^u$ and $\hat{\mathcal{N}}^b$, which include nonlinear and molecular viscous and dissipative terms, are given by

$$\begin{aligned}\hat{\mathcal{N}}^u &= \overline{(\boldsymbol{u}\cdot\boldsymbol{\nabla})\boldsymbol{u}}-(\boldsymbol{u}\cdot\boldsymbol{\nabla})\boldsymbol{u}+\frac{1}{\overline{\rho}}\left(\boldsymbol{j}\times\boldsymbol{b}-\overline{\boldsymbol{j}\times\boldsymbol{b}}\right)+\boldsymbol{f}_\nu(\boldsymbol{u}),\\ \hat{\mathcal{N}}^b &= \boldsymbol{\nabla}\times\left(\boldsymbol{u}\times\boldsymbol{b}-\overline{\boldsymbol{u}\times\boldsymbol{b}}-\eta\boldsymbol{\nabla}\times\boldsymbol{b}\right),\end{aligned}$$

where $\overline{\rho}\boldsymbol{f}_\nu(\boldsymbol{u})$ is the molecular viscous force and $\boldsymbol{j}=\boldsymbol{\nabla}\times\boldsymbol{b}/\mu_0$ is the fluctuating current density. To eliminate the pressure term from the equation of motion (12) we calculate $\boldsymbol{\nabla}\times(\boldsymbol{\nabla}\times\boldsymbol{u})$. Then we rewrite the obtained equation and Eq. (13) in Fourier space.

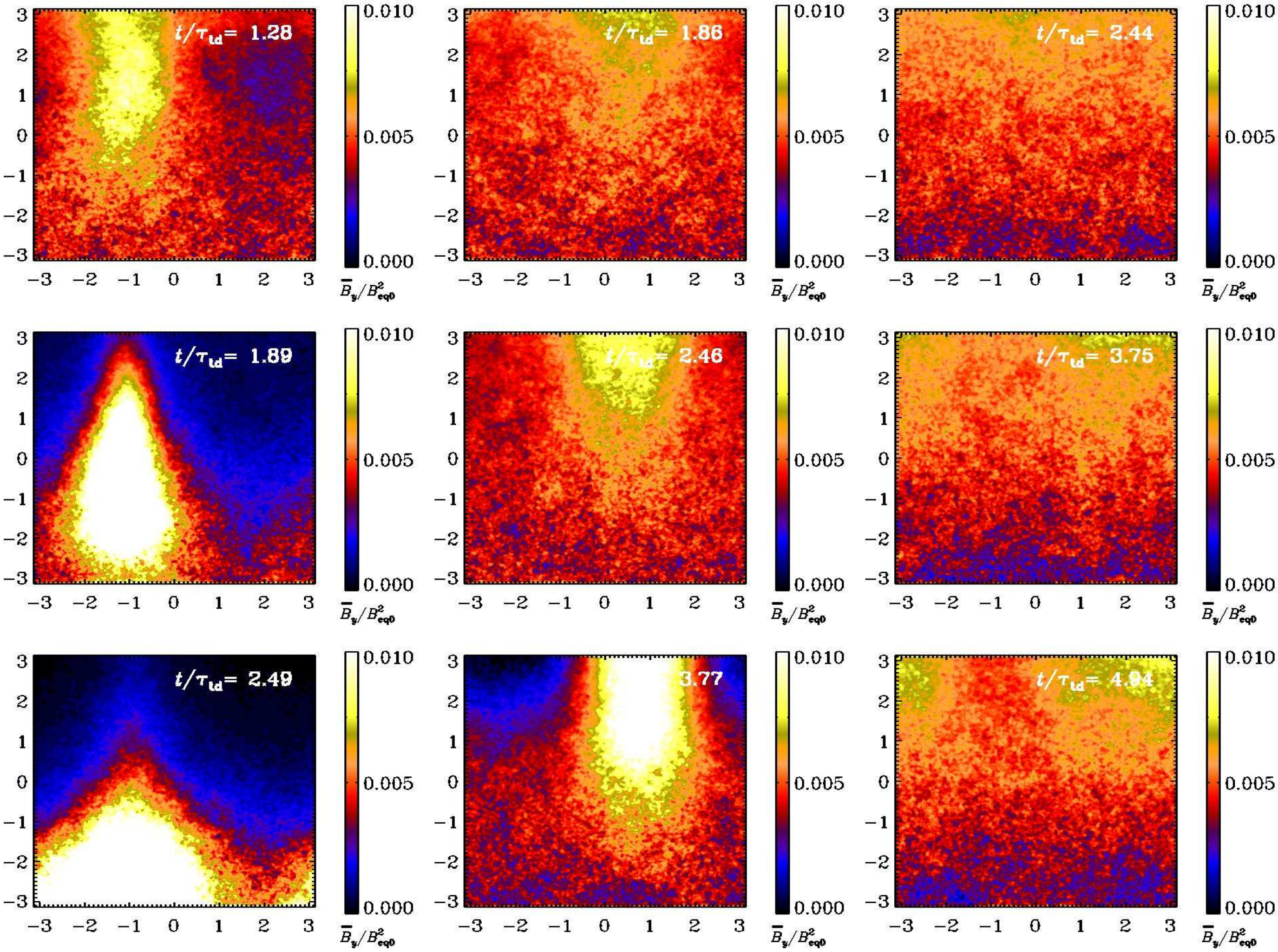

Fig. 2. yt-averaged $\overline{B}_y$ for Co $= 0.006$ (left), 0.03 (middle), and 0.06 (right) at different times.

4.2.2. Two-scale approach

We apply the two-scale approach and express two-point correlation functions in the following form

$$
\begin{aligned}
\overline{u_i(\boldsymbol{x})u_j(\boldsymbol{y})} &= \int d\boldsymbol{k}_1\, d\boldsymbol{k}_2\, \overline{u_i(\boldsymbol{k}_1)u_j(\boldsymbol{k}_2)}\exp\{i(\boldsymbol{k}_1\boldsymbol{\cdot}\boldsymbol{x}+\boldsymbol{k}_2\boldsymbol{\cdot}\boldsymbol{y})\}\\
&= \int d\boldsymbol{k}\, d\boldsymbol{K}\, f_{ij}(\boldsymbol{k},K)\exp(i\boldsymbol{k}\boldsymbol{\cdot}\boldsymbol{r}+i\boldsymbol{K}\boldsymbol{\cdot}\boldsymbol{R})\\
&= \int d\boldsymbol{k}\, f_{ij}(\boldsymbol{k},R)\exp(i\boldsymbol{k}\boldsymbol{\cdot}\boldsymbol{r}) \qquad (14)
\end{aligned}
$$

(see, e.g., Roberts & Soward, 1975). Here and elsewhere, we drop the common argument t in the correlation functions, $f_{ij}(\boldsymbol{k},R)=\hat{L}(u_i;u_j)$, where

$$\hat{L}(a;c) = \int \overline{a(\boldsymbol{k}+\boldsymbol{K}/2)c(-\boldsymbol{k}+\boldsymbol{K}/2)}\exp\left(i\boldsymbol{K}\boldsymbol{\cdot}\boldsymbol{R}\right)d\boldsymbol{K},$$

with the new variables $\boldsymbol{R}=(\boldsymbol{x}+\boldsymbol{y})/2$, $\boldsymbol{r}=\boldsymbol{x}-\boldsymbol{y}$, $\boldsymbol{K}=\boldsymbol{k}_1+\boldsymbol{k}_2$, $\boldsymbol{k}=(\boldsymbol{k}_1-\boldsymbol{k}_2)/2$. The variables $\boldsymbol{R}$ and $\boldsymbol{K}$ correspond to the large scales, while $\boldsymbol{r}$ and $\boldsymbol{k}$ correspond to the small scales. This implies that we have assumed that there exists a separation of scales, i.e., the turbulent forcing scale $\ell_{\rm f}$ is much smaller than the characteristic scale L_B of inhomogeneity of the mean magnetic field.

4.2.3. Equations for the second moments

We derive equations for the following correlation functions: $f_{ij}(\boldsymbol{k},R) = \hat{L}(u_i;u_j)$, $h_{ij}(\boldsymbol{k},R) = \overline{\rho}^{-1}\,\hat{L}(b_i;b_j)$ and $g_{ij}(\boldsymbol{k},R)=\hat{L}(b_i;u_j)$. The equations for these correlation functions are given by

$$\frac{\partial f_{ij}(\boldsymbol{k})}{\partial t} = i(\boldsymbol{k}\boldsymbol{\cdot}\overline{\boldsymbol{B}})\Phi_{ij} + L^{\Omega}_{ijmn}f_{mn} + I^f_{ij} + \hat{\mathcal{N}}^f, \qquad (15)$$

$$\frac{\partial h_{ij}(\boldsymbol{k})}{\partial t} = -i(\boldsymbol{k}\boldsymbol{\cdot}\overline{\boldsymbol{B}})\Phi_{ij} + I^h_{ij} + \hat{\mathcal{N}}^h, \qquad (16)$$

$$
\begin{aligned}
\frac{\partial g_{ij}(\boldsymbol{k})}{\partial t} &= i(\boldsymbol{k}\boldsymbol{\cdot}\overline{\boldsymbol{B}})[f_{ij}(\boldsymbol{k}) - h_{ij}(\boldsymbol{k}) - h^{(H)}_{ij}]\\
&\quad + D^{\Omega}_{jm}(\boldsymbol{k}_2)g_{im}(\boldsymbol{k}) + I^g_{ij} + \hat{\mathcal{N}}^g, \qquad (17)
\end{aligned}
$$

where

$$
\begin{aligned}
\Phi_{ij}(\boldsymbol{k}) &= \overline{\rho}^{-1}\,[g_{ij}(\boldsymbol{k}) - g_{ji}(-\boldsymbol{k})],\\
D^{\Omega}_{ij}(\boldsymbol{k}) &= 2\varepsilon_{ijm}\Omega_n k_{mn},\\
L^{\Omega}_{ijmn} &= D^{\Omega}_{im}(\boldsymbol{k}_1)\,\delta_{jn} + D^{\Omega}_{jn}(\boldsymbol{k}_2)\,\delta_{im}.
\end{aligned}
$$

Hereafter we have omitted the $\boldsymbol{R}$-argument in the correlation functions and neglected terms $\sim O(\nabla^2_{\boldsymbol{R}})$, and ε_{ijn} is the fully antisymmetric Levi-Civita tensor. In Eqs. (15)–(17), the terms

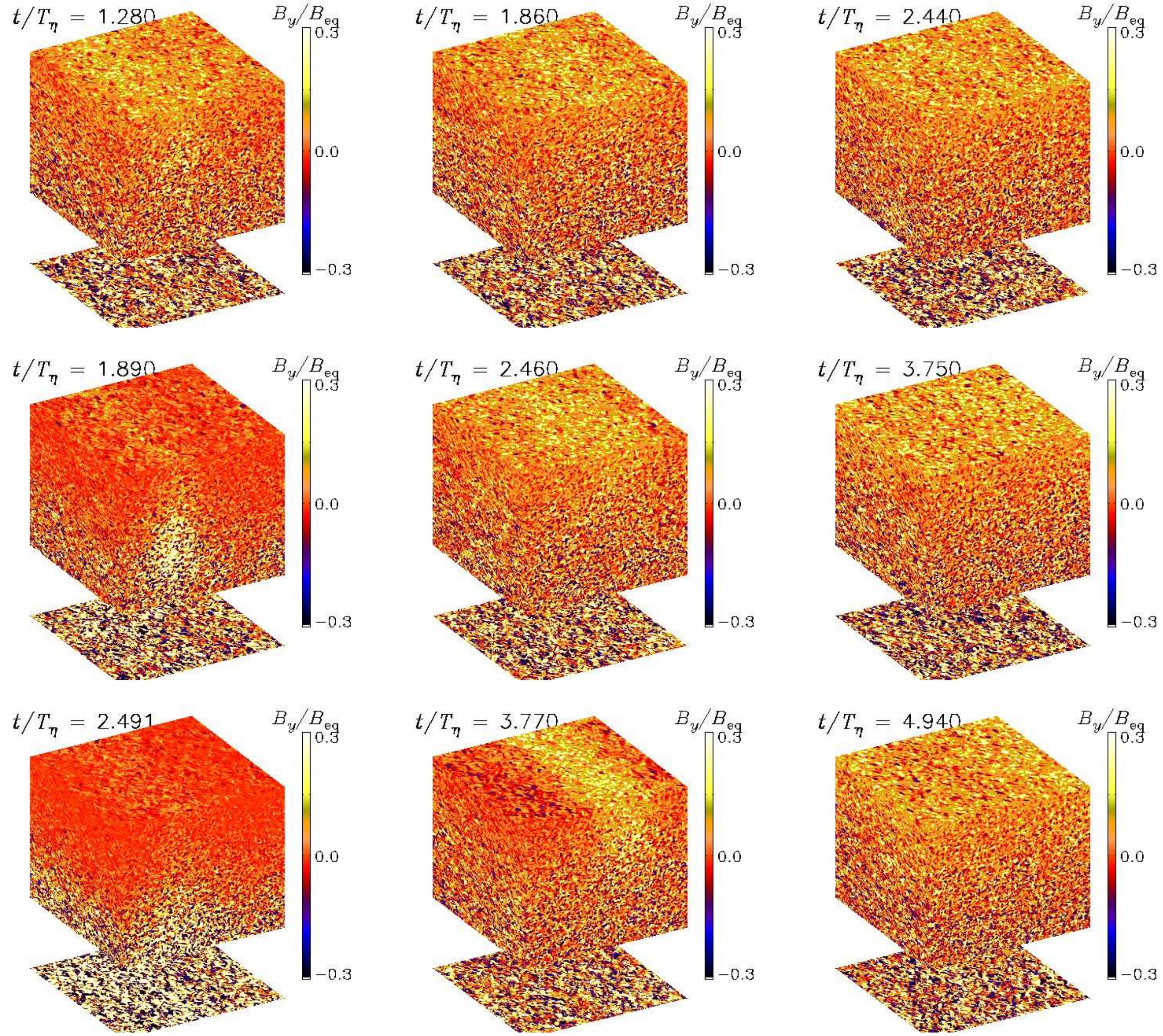

Fig. 3. B_y at the periphery of the computational domain for Co $= 0.006$ (left), 0.03 (middle), and 0.06 (right) at the same times as in Fig. 2. Note the strong surface effect for Co $= 0.03$ in the last time frame.

$\hat{\mathcal{N}}^f$, $\hat{\mathcal{N}}^h$ and $\hat{\mathcal{N}}^g$ are determined by the third moments appearing due to the nonlinear terms, the source terms I_{ij}^f , I_{ij}^h and I_{ij}^g which contain the large-scale spatial derivatives of the mean magnetic and velocity fields, are given by Eqs. (A3)–(A6) in Rogachevskii & Kleeorin (2004). These terms determine turbulent magnetic diffusion and effects of nonuniform mean velocity on the mean electromotive force.

For the derivation of Eqs. (15)–(17) we use an approach that is similar to that applied in Rogachevskii & Kleeorin (2004). We take into account that in Eq. (17) the terms with tensors that are symmetric in i and j do not contribute to the mean electromotive force because $\mathcal{E}_m = \varepsilon_{mji}\, g_{ij}$. We split all tensors into nonhelical, h_{ij}, and helical, $h_{ij}^{(H)}$, parts. The helical part of the tensor of magnetic fluctuations $h_{ij}^{(H)}$ depends on the magnetic helicity, and the equation for $h_{ij}^{(H)}$ follows from magnetic helicity conservation arguments (see, e.g., Kleeorin & Rogachevskii, 1999; Brandenburg & Subramanian, 2005a, and references therein).

4.2.4. τ-approach

The second-moment equations (15)–(17) include the first-order spatial differential operators applied to the third-order moments $M^{(\rm III)}$. To close the system, we express the set of the third-order terms $\hat{\mathcal{N}}^M \equiv \hat{\mathcal{N}} M^{(\rm III)}$ through the lower moments $M^{(\rm II)}$. We use the spectral τ approximation which postulates that the deviations of the third-moment terms, $\hat{\mathcal{N}} M^{(\rm III)}(\boldsymbol{k})$, from the contributions to these terms afforded by the background turbulence, $\hat{\mathcal{N}} M^{(\rm III,0)}(\boldsymbol{k})$, are expressed through similar deviations of the second moments:

$$\hat{\mathcal{N}} M^{(\rm III)}(\boldsymbol{k}) - \hat{\mathcal{N}} M^{(\rm III,0)}(\boldsymbol{k}) = -\frac{M^{(\rm II)}(\boldsymbol{k}) - M^{(\rm II,0)}(\boldsymbol{k})}{\tau(k)}$$

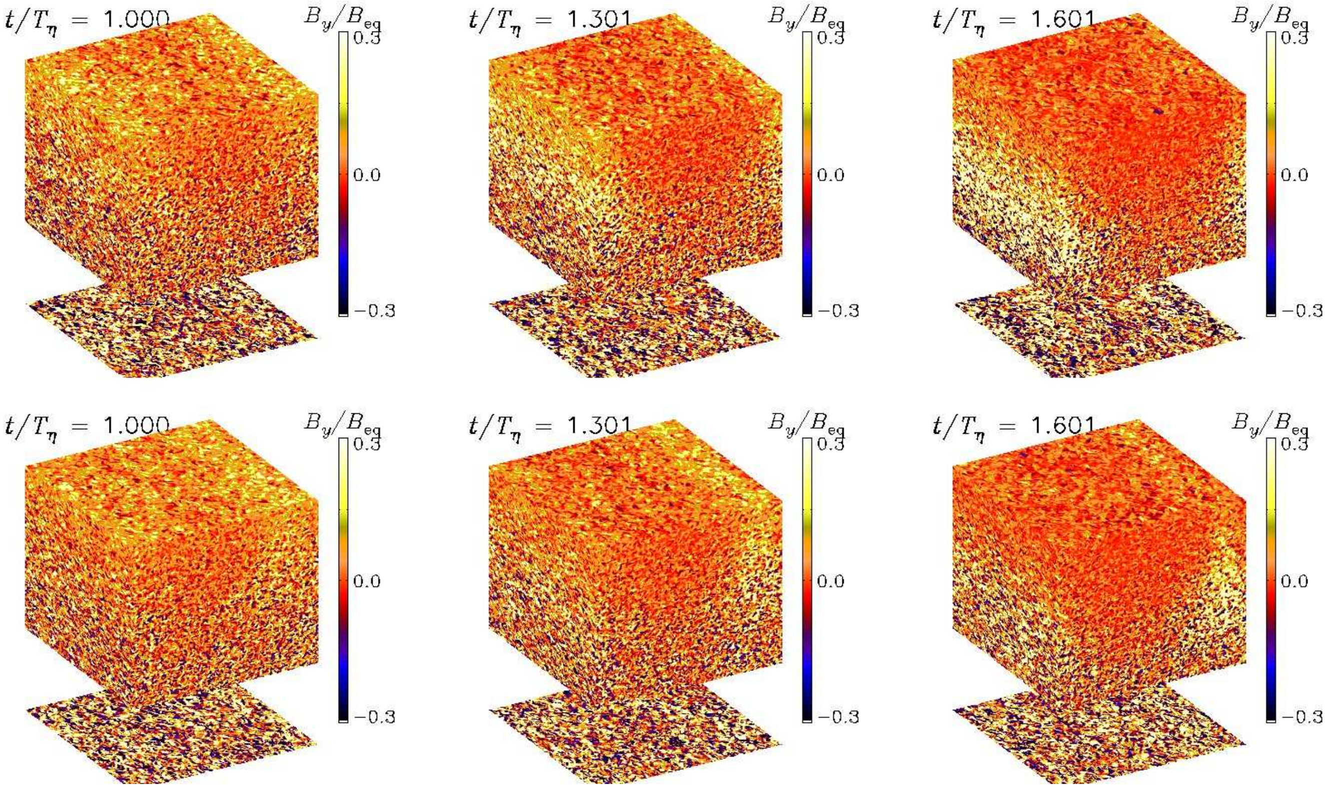

Fig. 4. B_y at the periphery of the computational domain for Co $= 0.006$ and $\theta = 45^\circ$ (upper row) and 90° (lower row), at three different times (from left to right).

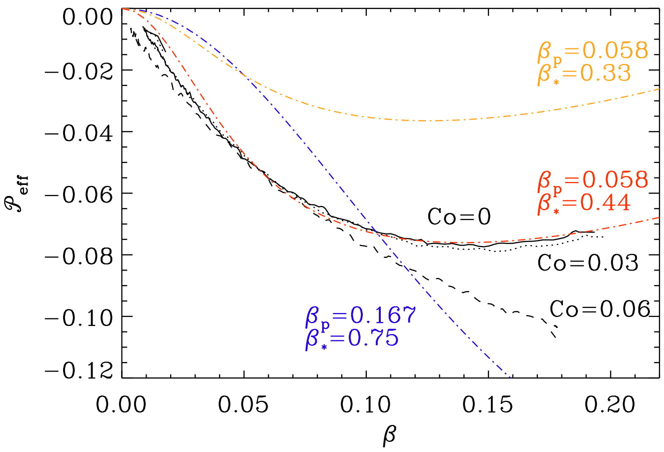

Fig. 5. Normalized effective magnetic pressure, $\mathcal{P}_{\rm eff}(\beta)$, for three values of Co, compared with Eq. (9) for different combinations of $\beta_\star$ and $\beta_{\rm p}$, as discussed in the text.

(18)

(Orszag, 1970; Pouquet et al., 1976; Kleeorin et al., 1990; Rogachevskii & Kleeorin, 2004), where $\tau(k)$ is the scale-dependent relaxation time, which can be identified with the correlation time of the turbulent velocity field for large Reynolds numbers. The quantities with the superscript (0) correspond to the background turbulence (see below). We apply the spectral τ approximation only for the nonhelical part h_{ij} of the tensor of magnetic fluctuations. A justification for the τ approximation in different situations has been offered through numerical simulations and analytical studies (see, e.g., Brandenburg et al., 2004; Brandenburg & Subramanian, 2005b, 2007; Rogachevskii et al., 2011).

4.2.5. Solution of equations for the second moments

We solve Eqs. (15)–(17) neglecting the sources $I^f_{ij}, I^h_{ij}, I^g_{ij}$ with the large-scale spatial derivatives. The terms with the large-scale spatial derivatives which determine the turbulent magnetic diffusion, can be taken into account by perturbations. We subtract from Eqs. (15)–(17) the corresponding equations written for the background turbulence, use the spectral τ approximation. We assume that the characteristic time of variation of the second moments is substantially larger than the correlation time $\tau(k)$ for all turbulence scales. This allows us to get a stationary solution for the equations for the second-order moments, $M^{\rm (II)}$. Thus, we arrive to the following steady-state solution of Eqs. (15)–(17):

$$f_{ij}(\boldsymbol{k}) = L^{-1}_{ijmn}\left[f^{(0)}_{mn}(\boldsymbol{k}) + i\tau(\boldsymbol{k}\cdot\overline{\boldsymbol{B}})\Phi_{mn}(\boldsymbol{k})\right], \qquad (19)$$

$$h_{ij}(\boldsymbol{k}) = -i\tau(\boldsymbol{k}\cdot\overline{\boldsymbol{B}})\Phi_{ij}(\boldsymbol{k}), \qquad (20)$$

$$g_{ij}(\boldsymbol{k}) = i\tau(\boldsymbol{k}\cdot\overline{\boldsymbol{B}})D^{-1}_{im}\left[f_{mj}(\boldsymbol{k}) - h_{mj}(\boldsymbol{k})\right]. \qquad (21)$$

We have assumed that there is no small-scale dynamo in the background turbulence. Here the operator D^{-1}_{ij} is the inverse of the operator $\delta_{ij} - \tau D^{\Omega}_{ij}$ (Rädler et al., 2003) and the operator L^{-1}_{ijmn} is the inverse of the operator $\delta_{im}\delta_{jn} - \tau\, L^{\Omega}_{ijmn}$ (Elperin et al., 2005). These operators are given by

$$D^{-1}_{ij} = \chi(\psi)\,(\delta_{ij} + \psi\,\varepsilon_{ijm}\,\hat{k}_m + \psi^2\,k_{ij})$$

$$= \delta_{ij} + \psi\, \varepsilon_{ijm}\, \hat{k}_m - \psi^2\, P_{ij} + O(\psi^3), \qquad (22)$$

$$L^{-1}_{ijmn}(\boldsymbol{\Omega}) = \tfrac{1}{2}[B_1\, \delta_{im}\delta_{jn} + B_2\, k_{ijmn} + B_3\, (\varepsilon_{imp}\delta_{jn}$$
$$+\varepsilon_{jnp}\delta_{im})\hat{k}_p + B_4\, (\delta_{im}k_{jn} + \delta_{jn}k_{im})$$
$$+B_5\, \varepsilon_{ipm}\varepsilon_{jqn}k_{pq} + B_6\, (\varepsilon_{imp}k_{jpn} + \varepsilon_{jnp}k_{ipm})]$$
$$= \delta_{im}\delta_{jn} + \psi\, (\varepsilon_{imp}\delta_{jn} + \varepsilon_{jnp}\delta_{im})\hat{k}_p - \psi^2(\delta_{im}P_{jn}$$
$$+\delta_{jn}P_{im} - 2\varepsilon_{imp}\varepsilon_{jqn}k_{pq}) + O(\psi^3), \qquad (23)$$

where $\hat{k}_i = k_i/k,\ \chi(\psi) = 1/(1+\psi^2),\ \psi = 2\tau(k)\,(\boldsymbol{k}\cdot\boldsymbol{\Omega})/k$, $B_1 = 1+\chi(2\psi),\ B_2 = B_1 + 2 - 4\chi(\psi),\ B_3 = 2\psi\,\chi(2\psi)$, $B_4 = 2\chi(\psi) - B_1,\ B_5 = 2 - B_1$ and $B_6 = 2\psi\,[\chi(\psi) - \chi(2\psi)]$, $P_{ij}(k) = \delta_{ij} - k_i k_j/k^2$, δ_{ij} is the Kronecker tensor.

We use the following model for the homogeneous and isotropic background turbulence: $f^{(0)}_{ij}(\boldsymbol{k}) = \langle \boldsymbol{u}^2\rangle\, P_{ij}(k)\, W(k)$, where $W(k) = E(k)/8\pi k^2$, the energy spectrum is $E(k) = (q-1)k_0^{-1}(k/k_0)^{-q}$, $k_0 = 1/\ell_{\rm f}$ and the length $\ell_{\rm f}$ is the maximum scale of turbulent motions. The turbulent correlation time is $\tau(k) = C\,\tau_0\,(k/k_0)^{-\mu}$, where the coefficient $C = (q - 1 + \mu)/(q-1)$. This value of the coefficient C corresponds to the standard form of the turbulent diffusion coefficient in the isotropic case, i.e., $\eta_{_T} = \langle \boldsymbol{u}^2\rangle \int \tau(k)\, E(k)\, dk = \tau_0\, \langle \boldsymbol{u}^2\rangle/3$. Here the time $\tau_0 = \ell_{\rm f}/\sqrt{\langle \boldsymbol{u}^2\rangle}$ and $\sqrt{\langle \boldsymbol{u}^2\rangle}$ is the characteristic turbulent velocity in the scale $\ell_{\rm f}$. For the Kolmogorov's type background turbulence (i.e., for a turbulence with a constant energy flux over the spectrum), the exponent $\mu = q-1$ and the coefficient $C = 2$. In the case of a turbulence with a scale-independent correlation time, the exponent $\mu = 0$ and the coefficient $C = 1$. Motions in the background turbulence are assumed to be non-helical.

Equations (19)–(23) yield:

$$f_{ij}(\boldsymbol{k}) = f^{(0)}_{ij}(\boldsymbol{k}) - h_{ij}(\boldsymbol{k}), \qquad (24)$$

$$h_{ij}(\boldsymbol{k}) = \frac{\Psi}{1+2\Psi}\left(1 - \psi^2 \frac{2+\Psi}{2(1+2\Psi)}\right) f^{(0)}_{ij}(\boldsymbol{k}), \qquad (25)$$

where $\Psi = 2\tau^2(\boldsymbol{k}\boldsymbol{\cdot}\boldsymbol{c}_A)^2$, $\boldsymbol{c}_A = \overline{\boldsymbol{B}}/\sqrt{\rho}$, and we have taken into account that $L^{-1}_{ijmn}P_{mn}(\boldsymbol{k}) = P_{ij}(\boldsymbol{k})$. After the integration in $\boldsymbol{k}$ space we obtain the magnetic tensor h_{ij} in physical space:

$$h_{ij}(\beta) = q_1(\beta)\delta_{ij} + q_2(\beta)\beta_{ij}, \qquad (26)$$

where $\beta = \overline{B}/B_{\rm eq}$, and the functions $q_1(\beta)$ and $q_2(\beta)$ are given in Appendix B. We consider the case in which the angular velocity is perpendicular to the mean magnetic field. The results can easily be generalized to the case of the arbitrary angle between the angular velocity and the mean magnetic field.

The contribution of turbulence to the mean-field magnetic pressure is given by the function $q_{\rm p}(\beta) = [q_1(\beta) - q_2(\beta)]\,/\beta^2$:

$$q_{\rm p}(\beta) = \frac{1}{12\beta^2}\Big[A_1^{(0)}(0) - A_1^{(0)}(4\beta) - A_2^{(0)}(4\beta)$$
$$-2(\Omega\tau_0)^2\Big(A_1^{(2)}(0) - 4C_1^{(2)}(0) - 10A_1^{(2)}(4\beta)$$
$$+40C_1^{(2)}(4\beta) + \frac{9}{2\pi}\left[\bar{A}_1(16\beta^2) - 4\bar{C}_1(16\beta^2)\right]\Big)\Big], \qquad (27)$$

where the functions $A_i^{(j)}(x)$, $C_i^{(j)}(x)$, $\bar{A}_i(y)$ and $\bar{C}_i(y)$, and their asymptotics are given in Appendix B. Following earlier work (Brandenburg et al., 2012a), we now define a magnetic Reynolds number based on the scale $\ell_{\rm f} = 2\pi/k_{\rm f}$, which is related to the ${\rm Re}_M$ defined earlier via ${\rm Rm} = 2\pi{\rm Re}_M$. For $\overline{B} \ll B_{\rm eq}/4{\rm Rm}^{1/4}$, the function $q_{\rm p}(\beta)$ is given by

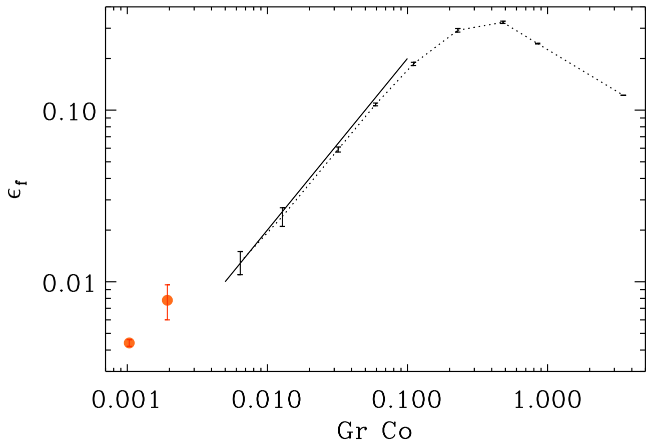

Fig. 6. Relative kinetic helicity spectrum as a function of GrCo (red symbols) compared with results from earlier simulations of Brandenburg et al. (2012b).

$$q_{\rm p}(\beta) = \frac{4}{5}\ln{\rm Rm} - \frac{8}{35}{\rm Co}^2, \qquad (28)$$

and for $B_{\rm eq}/4{\rm Rm}^{1/4} \ll \overline{B} \ll B_{\rm eq}/4$ the function $q_{\rm p}(\beta)$ is given by

$$q_p(\beta) \;=\; \frac{16}{25}\,\left(1 + 5|\ln(4\beta)| + 32\,\beta^2\right) - \frac{8}{35}{\rm Co}^2, \qquad (29)$$

where ${\rm Co} = 2\Omega\tau_0$. This shows that for the values of Co of interest (${\rm Co} \leq 0.06$), the correction to $q_{\rm p}$ is negligible (below 10^{-3}), which is in agreement with the numerical findings in Fig. 5.

5. Kinetic and magnetic helicity

5.1. Helicity production

In turbulence, the presence of rotation and stratification gives rise to kinetic helicity and an α effect (Krause & Rädler, 1980; Brandenburg et al., 2013). As a measure of kinetic helicity, we determine the normalized helicity

$$\epsilon_{\rm f} = \overline{\boldsymbol{\omega}\cdot\boldsymbol{u}}/k_{\rm f}u_{\rm rms}^2. \qquad (30)$$

In Fig. 6 we compare two of our present runs at $k_{\rm f}/k_1 = 30$ with those of Brandenburg et al. (2012b) at $k_{\rm f}/k_1 = 5$ showing $\epsilon_{\rm f}$ versus Gr Co. For our present runs (red open symbols), kinetic helicity is clearly very small, which is a consequence of the small value of Co. Compared with earlier runs at $k_{\rm f}/k_1 = 5$, which gave $\epsilon_{\rm f} \approx 2\,{\rm Gr\,Co}$, the present ones show about twice as much helicity. Interestingly, in the limit of rapid rotation the relative kinetic helicity declines again when the product Gr Co is larger than about 0.5. The maximum value of $\epsilon_{\rm f}$ that can be reached is about 0.3.

5.2. Surface diagnostics

As a consequence of the production of kinetic helicity, the magnetic field should also be helical. However, since magnetic helicity is conserved, and since it was zero initially, it should remain zero – at least on a dynamical time scale (Berger, 1984). This condition can be obeyed if the magnetic field is bi-helical,

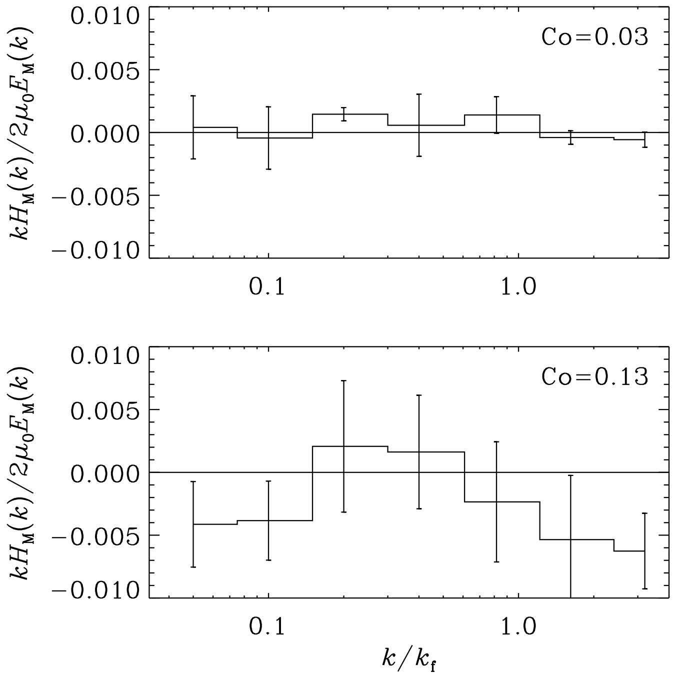

Fig. 7. Normalized magnetic helicity spectrum for Co $= 0.03$ (upper panel) and Co $= 0.13$ (lower panel).

i.e., with opposite signs of magnetic helicity at large and small wavenumbers (Seehafer, 1996; Ji, 1999). We may now ask whether signatures of this could in principle be detected at the solar surface. To address this question, we use our simulation at intermediate rotation speed with Co $= 0.03$, where magnetic flux concentrations are well developed at the surface of the domain, and compare with a larger value of 0.13.

Measuring magnetic helicity is notoriously difficult, because it involves the magnetic vector potential which is gauge dependent. However, under the assumption of homogeneity and isotropy, the Fourier transform of the magnetic correlation tensor is

$$M_{ij}(\boldsymbol{k}) = (\delta_{ij} - \hat{k}_i\hat{k}_j)\,\frac{\mu_0 E_{\rm M}(k)}{4\pi k^2} - \epsilon_{ijk}\frac{{\rm i}k_k H_{\rm M}(k)}{8\pi k^2}, \qquad (31)$$

where $\hat{\boldsymbol{k}} = \boldsymbol{k}/k$ is the unit vector of $\boldsymbol{k}$, and $E_{\rm M}(k)$ and $H_{\rm M}(k)$ are magnetic energy and magnetic helicity spectra, which obey the realizability condition, $2\mu_0 E_{\rm M}(k) \geq k|H_{\rm M}(k)|$, where the factor 2 in front of $E_{\rm M}(k)$ is just a consequence of the factor 1/2 in the definition of energy. Matthaeus et al. (1982) used the solar wind data from *Voyager II* to determine $H_{\rm M}(k)$ from the *in situ* measurements of $\boldsymbol{B}$ and Brandenburg et al. (2011b) applied it to measuring $H_{\rm M}(k)$ at high heliographic latitudes where $H_{\rm M}(k)$ is finite and turned out to be bi-helical. We now adopt the same method using Fourier transforms in the y direction. In the Sun, this corresponds to measuring $\boldsymbol{B}$ along a 2π ring at fixed polar latitude. In Fig. 7 we show the result for two values of Co.

It turns out that $H_{\rm M}(k)$ is compatible with zero for our intermediate value of Co. For faster rotation (Co $= 0.13$), $H_{\rm M}(k)$ is negative both at large wavenumbers ($k \gg k_{\rm f}$), and positive (but still compatible with zero within error bars) at intermediate wavenumbers ($0.15 < k/k_{\rm f} < 0.6$). For $k/k_{\rm f} < 0.15$, the magnetic helicity is again negative. However, the error bars are large and rotation is already so fast that structure formation via NEMPI is impossible. It is therefore unclear whether meaningful conclusions can be drawn from our results. By comparison, a bi-helicity is expected in the northern hemisphere of the Sun, where magnetic helicity is negative on all scales except the largest ones where the α effect operates. In this connection we remind the reader that this sense is reversed in the solar wind far from the Sun (Brandenburg et al., 2011b). This has also been seen in simulations of magnetic ejecta from a dynamo-active sphere (Warnecke et al., 2011), which may be explained by a diffusive magnetic helicity transport (Warnecke et al., 2012).

6. Conclusions and discussion

The present work has confirmed the rather stringent restrictions of LBKMR showing that NEMPI is suppressed already for rather weak rotation (Co $\gtrsim 0.03$). Applied to the Sun with $\Omega = 2\times10^{-6}\,{\rm s}^{-1}$, this implies that NEMPI can only play a role in the upper-most layers where the correlation time is shorter than ${\rm Co}/2\Omega \approx 2$ hours. This is surprising as it does exclude even the lower parts of the supergranulation layer where τ is of the order of 1 day. On the other hand, we have to keep in mind that our conclusions based on isothermal models, should be taken with care. It would therefore be useful to extend the present studies to polytropic layers where the scale height varies with depth. It should also be noted that weak rotation (Co $= 0.03$) seems to enhance the surface appearance. This would be compatible with an interpretation that rotation prevents structures from sinking. However, preliminary mean-field calculations do not indicate a significant dependence of the eigenfunction on Co for values below 0.1. Our interpretation, if correct, would therefore need to be a result of nonlinearity.

If we were to apply NEMPI to the formation of active regions in the Sun, we should keep in mind that the scale of structures would be 6–8 pressure scale heights (Kemel et al., 2012a). At the depth where the turnover time is about 2 hours, we estimate the rms velocity to be about 500 m/s, so the scale height would be about 3 Mm, corresponding to a NEMPI scale of at least 20 Mm. This might still be of interest for explaining plage regions in the Sun. Clearly, more work using realistic models would be required for making more conclusive statements.

Regarding the production of kinetic helicity and the possible detection of a magnetic helicity spectrum, our results suggest that the relative magnetic helicity cannot be expected to be more than about 0.01. This is a consequence of correspondingly low values of kinetic helicity. We find that the normalized kinetic helicity is given by $\epsilon_{\rm f} \approx 2{\rm Gr}\,{\rm Co}$. For the Sun, we expect ${\rm Gr} = (k_{\rm f}H_\rho)^{-1} \approx 0.16$ (see Appendix C), which agrees with what is used in our simulations, leaving therefore not much room for more optimistic estimates.

Acknowledgements. We thank Koen Kemel for helpful comments concerning the influence of magnetic structure formation on the measurement of $q_{\rm p0}$ and $\beta_{\rm p}$ in DNS. Illa R. Losada was supported by PhD Grant ‘Beca de Investigación CajaCanarias para Postgraduados 2011’. This work was supported in part by the European Research Council under the AstroDyn Research Project No. 227952, by the National Science Foundation under Grant No. NSF PHY05-51164 (AB), by EU COST Action MP0806, by the European Research Council under the Atmospheric Research Project No. 227915, and by a grant from the Government of the Russian Federation under contract No. 11.G34.31.0048 (NK, IR). We acknowledge the allocation of computing resources provided by the Swedish National Allocations Committee at the Center for Parallel Computers at the Royal Institute of Technology in Stockholm and the National Supercomputer Centers in Linköping.

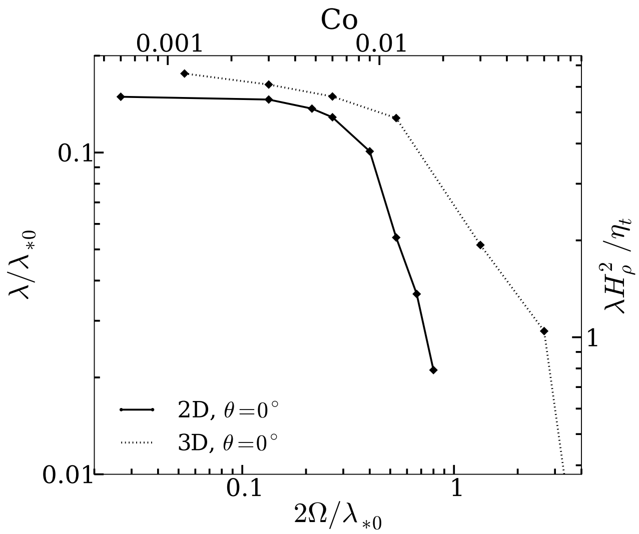

Fig. A.1. Dependence of λ/λ_{*0} on $2\Omega/\lambda_{*0}$ for $\theta = 0^\circ$ in the 3D and 2D cases for $\theta = 0$ (corresponding to the pole).

Appendix A: Revised comparison of the 2-D and 3-D data of LBKMR

We note that in Fig. 3 of LBKMR the growth rates from the 2-D calculations came out to be much smaller than in 3-D. This was however a mistake caused by determining the amplification of the total magnetic field (which included the imposed field), rather than the fluctuations of the magnetic field or the velocity. We use here the opportunity to present the revised plot in Fig. A.1.

Appendix B: The identities used in Sect. 4.2 for the integration in $\boldsymbol{k}$–space

To integrate over the angles in $\boldsymbol{k}$–space in Sect. 4.2 we used the following identities (Rogachevskii & Kleeorin, 2004, 2007):

$$\bar{K}_{ij} = \int \frac{k_{ij}\sin\theta}{1+a\cos^2\theta}\,d\theta\,d\varphi = \bar{A}_1\delta_{ij} + \bar{A}_2\beta_{ij}, \tag{B.1}$$

$$\begin{aligned}\bar{K}_{ijmn} = \int \frac{k_{ijmn}\sin\theta}{1+a\cos^2\theta}\,d\theta\,d\varphi = \bar{C}_1(\delta_{ij}\delta_{mn} + \delta_{im}\delta_{jn} \\ +\delta_{in}\delta_{jm}) + \bar{C}_2\beta_{ijmn} + \bar{C}_3(\delta_{ij}\beta_{mn} + \delta_{im}\beta_{jn} + \delta_{in}\beta_{jm} \\ +\delta_{jm}\beta_{in} + \delta_{jn}\beta_{im} + \delta_{mn}\beta_{ij}),\end{aligned} \tag{B.2}$$

$$\begin{aligned}\bar{H}_{ijmn}(a) &= \int \frac{k_{ijmn}\sin\theta}{(1+a\cos^2\theta)^2}\,d\theta\,d\varphi \\ &= -\left(\frac{\partial}{\partial b}\int \frac{k_{ijmn}\sin\theta}{b+a\cos^2\theta}\,d\theta\,d\varphi\right)_{b=1} \\ &= \bar{K}_{ijmn}(a) + a\frac{\partial}{\partial a}\bar{K}_{ijmn}(a)\ ,\end{aligned} \tag{B.3}$$

where $\hat{\beta}_i = \beta_i/\beta$, $\beta_{ij} = \hat{\beta}_i\hat{\beta}_j$, and

$$\begin{aligned}\bar{A}_1 &= \frac{2\pi}{a}\left[(a+1)\frac{\arctan(\sqrt{a})}{\sqrt{a}} - 1\right]\ , \\ \bar{A}_2 &= -\frac{2\pi}{a}\left[(a+3)\frac{\arctan(\sqrt{a})}{\sqrt{a}} - 3\right]\ , \\ \bar{C}_1 &= \frac{\pi}{2a^2}\left[(a+1)^2\frac{\arctan(\sqrt{a})}{\sqrt{a}} - \frac{5a}{3} - 1\right]\ , \\ \bar{C}_2 &= \bar{A}_2 - 7\bar{A}_1 + 35\bar{C}_1\ , \\ \bar{C}_3 &= \bar{A}_1 - 5\bar{C}_1\ .\end{aligned} \tag{B.4}$$

In the case of $a \ll 1$ these functions are given by

$$\begin{aligned}\bar{A}_1(a) &\sim \frac{4\pi}{3}\left(1-\frac{1}{5}a\right)\ , \quad \bar{A}_2(a) \sim -\frac{8\pi}{15}a\ , \\ \bar{C}_1(a) &\sim \frac{4\pi}{15}\left(1-\frac{1}{7}a\right).\end{aligned}$$

In the case of $a \gg 1$ these functions are given by

$$\begin{aligned}\bar{A}_1(a) &\sim \frac{\pi^2}{\sqrt{a}} - \frac{4\pi}{a}\ , \quad \bar{A}_2(a) \sim -\frac{\pi^2}{\sqrt{a}} + \frac{8\pi}{a}\ , \\ \bar{C}_1(a) &\sim \frac{\pi^2}{4\sqrt{a}} - \frac{4\pi}{3a}.\end{aligned}$$

The functions $A_n^{(m)}(\tilde\beta)$ are given by

$$A_n^{(0)}(\tilde\beta) = \frac{3\tilde\beta^2}{\pi}\int_{\tilde\beta}^{\tilde\beta\mathrm{Rm}^{1/4}} \frac{\bar{A}_n(X^2)}{X^3}\,dX\ , \tag{B.5}$$

$$A_n^{(2)}(\tilde\beta) = \frac{3\tilde\beta^6}{\pi}\int_{\tilde\beta}^{\tilde\beta\mathrm{Rm}^{1/4}} \frac{\bar{A}_n(X^2)}{X^7}\,dX, \tag{B.6}$$

$$\int_0^1 \bar{A}_n(a(\bar\tau))\bar\tau^m\,d\bar\tau = \frac{2\pi}{3}A_n^{(m)}(\tilde\beta), \tag{B.7}$$

and similarly for $C_n^{(m)}(\tilde\beta)$, where $a = [\tilde\beta u_0 k\tau(k)/2]^2$, $\tilde\beta = \sqrt{8}\ \overline{B}/B_{\rm eq}$, and $X^2 = \tilde\beta^2(k/k_0)^{2/3} = \tilde\beta^2/\bar\tau = a$. The explicit form of the functions $A_n^{(m)}(\tilde\beta)$ and $C_n^{(m)}(\tilde\beta)$ for $m = 0;\ 2$ are given by

$$\begin{aligned}A_1^{(0)}(\tilde\beta) &= \frac{1}{5}\biggl[2 + 2\frac{\arctan\tilde\beta}{\tilde\beta^3}(3+5\tilde\beta^2) - \frac{6}{\tilde\beta^2} - \tilde\beta^2\ln\mathrm{Rm} \\ &\quad -2\tilde\beta^2\ln\left(\frac{1+\tilde\beta^2}{1+\tilde\beta^2\sqrt{\mathrm{Rm}}}\right)\biggr],\end{aligned} \tag{B.8}$$

$$\begin{aligned}A_2^{(0)}(\tilde\beta) &= \frac{2}{5}\biggl[2 - \frac{\arctan\tilde\beta}{\tilde\beta^3}(9+5\tilde\beta^2) + \frac{9}{\tilde\beta^2} - \tilde\beta^2\ln\mathrm{Rm} \\ &\quad -2\tilde\beta^2\ln\left(\frac{1+\tilde\beta^2}{1+\tilde\beta^2\sqrt{\mathrm{Rm}}}\right)\biggr],\end{aligned} \tag{B.9}$$

$$A_1^{(2)}(\tilde\beta) = \frac{2}{63}\left[1 + 3\frac{\arctan\tilde\beta}{\tilde\beta^3}(7+9\tilde\beta^2) - \frac{21}{\tilde\beta^2} - \frac{3\tilde\beta^2}{2}M(\tilde\beta)\right], \tag{B.10}$$

$$\begin{aligned}C_1^{(2)}(\tilde\beta) &= \frac{1}{33}\biggl[\frac{2}{21} + \frac{\arctan\tilde\beta}{\tilde\beta^5}\left(\frac{99}{14}\tilde\beta^4 + 11\tilde\beta^2 + \frac{9}{2}\right) \\ &\quad -\frac{19}{2\tilde\beta^2} - \frac{9}{2\tilde\beta^4} - \frac{\tilde\beta^2}{7}M(\tilde\beta)\biggr],\end{aligned} \tag{B.11}$$

where $M(\tilde\beta) = 1 - 2\tilde\beta^2 + 2\tilde\beta^4\ln(1+\tilde\beta^{-2})$. Here we have taken into account that $\mathrm{Rm} \gg 1$. For $\overline{B} \ll B_{\rm eq}/4\mathrm{Rm}^{1/4}$ these functions are given by

$$\begin{aligned}A_1^{(0)}(\tilde\beta) &\sim 2 - \frac{1}{5}\tilde\beta^2\ln\mathrm{Rm}, \\ A_2^{(0)}(\tilde\beta) &\sim -\frac{2}{5}\tilde\beta^2\left[\ln\mathrm{Rm} + \frac{2}{15}\right], \\ A_1^{(2)}(\tilde\beta) &\sim \frac{2}{3}\left(1 - \frac{3}{10}\tilde\beta^2\right), \quad A_2^{(2)}(\tilde\beta) \sim -\frac{2}{5}\tilde\beta^2,\end{aligned}$$

$$C_1^{(2)}(\tilde{\beta}) \;\sim\; \frac{2}{15}\left(1-\frac{3}{14}\tilde{\beta}^2\right).$$

For $B_{\rm eq}/4{\rm Rm}^{1/4} \ll \overline{B} \ll B_{\rm eq}/4$ these functions are given by

$$A_1^{(0)}(\tilde{\beta}) \;\sim\; 2+\frac{2}{5}\tilde{\beta}^2\left[2\ln\tilde{\beta}-\frac{16}{15}+\frac{4}{7}\tilde{\beta}^2\right],$$

$$A_2^{(0)}(\tilde{\beta}) \;\sim\; \frac{2}{5}\tilde{\beta}^2\left[4\ln\tilde{\beta}-\frac{2}{15}-3\tilde{\beta}^2\right].$$

Other functions in this case have the same asymptotics as in the case of $\overline{B} \ll B_{\rm eq}/4{\rm Rm}^{1/4}$. For $B \gg B_{\rm eq}/4$ these functions are given by

$$A_1^{(0)}(\tilde{\beta}) \;\sim\; \frac{\pi}{\tilde{\beta}}-\frac{3}{\tilde{\beta}^2}, \quad A_2^{(0)}(\tilde{\beta}) \sim -\frac{\pi}{\tilde{\beta}}+\frac{6}{\tilde{\beta}^2},$$

$$A_1^{(2)}(\tilde{\beta}) \;\sim\; \frac{3\pi}{7\tilde{\beta}}-\frac{3}{2\tilde{\beta}^2}, \quad A_2^{(2)}(\tilde{\beta}) \sim -\frac{3\pi}{7\tilde{\beta}}+\frac{3}{\tilde{\beta}^2},$$

$$C_1^{(2)}(\tilde{\beta}) \;\sim\; \frac{3\pi}{28\tilde{\beta}}-\frac{1}{2\tilde{\beta}^2}.$$

The functions $q_1(\beta)$ and $q_2(\beta)$ are given by

$$\begin{aligned} q_1(\beta) = {}& \frac{1}{12}\Big[A_1^{(0)}(0)-A_1^{(0)}(4\beta)-\tfrac{1}{2}A_2^{(0)}(4\beta) \\ & -(\Omega\tau_0)^2\Big(A_1^{(2)}(0)-2C_1^{(2)}(0)-10A_1^{(2)}(4\beta) \\ & +20C_1^{(2)}(4\beta)+\frac{9}{2\pi}\left[\bar{A}_1(16\beta^2)-2\bar{C}_1(16\beta^2)\right]\Big)\Big], \end{aligned} \tag{B.12}$$

$$\begin{aligned} q_2(\beta) = {}& \frac{1}{12}\Big[\tfrac{1}{2}A_2^{(0)}(4\beta)+(\Omega\tau_0)^2\Big(A_1^{(2)}(0)-6C_1^{(2)}(0) \\ & -10A_1^{(2)}(4\beta)+60C_1^{(2)}(4\beta)+\frac{9}{2\pi}\big[\bar{A}_1(16\beta^2) \\ & -6\bar{C}_1(16\beta^2)\big]\Big)\Big], \end{aligned} \tag{B.13}$$

where $\beta=\overline{B}/B_{\rm eq}$.

Appendix C: Revised estimate for $k_{\rm f}H_\rho$

In Kemel et al. (2012a) the value of $k_{\rm f}H_\rho$ (= Gr^{-1}) was estimated based on stellar mixing length theory, using $\ell_{\rm mix}=\alpha_{\rm mix}H_p$ for the mixing length with $\alpha_{\rm mix}H_p\approx 1.6$ as an empirical parameter. For isentropic stratification, the pressure scale height H_p is related to H_ρ via $\gamma H_p\approx H_\rho$. With $k_{\rm f}=2\pi/\ell_{\rm mix}$ we obtain $k_{\rm f}H_\rho=2\pi\,\gamma/\alpha_{\rm mix}\approx 2\pi$, so Gr $=(k_{\rm f}H_\rho)^{-1}\approx 0.16$. Owing to a mistake, we underestimated in Kemel et al. (2012a) the value of $k_{\rm f}H_\rho$ by a factor of 2.6. The correct value of the growth rate of NEMPI should therefore be larger and would now be clearly faster than the turbulent–diffusive rate.

References

Berger, M. 1984, Geophys. Astrophys. Fluid Dyn., 30, 79
Brandenburg, A., & Subramanian, K. 2005a, Phys. Rep., 417, 1
Brandenburg, A., & Subramanian, K. 2005b, A&A, 439, 835
Brandenburg, A., & Subramanian, K. 2007, Astron. Nachr., 328, 507
Brandenburg, A., Käpylä, P., & Mohammed, A. 2004, Phys. Fluids, 16, 1020
Brandenburg, A., Kleeorin, N., Rogachevskii, I. 2010, Astron. Nachr., 331, 5
Brandenburg, A., Kemel, K., Kleeorin, N., Mitra, D., Rogachevskii, I. 2011a, ApJ, 740, L50
Brandenburg, A., Subramanian, K., Balogh, A., & Goldstein, M. L. 2011b, ApJ, 734, 9
Brandenburg, A., Kemel, K., Kleeorin, N., Rogachevskii, I. 2012a, ApJ, 749, 179
Brandenburg, A., Rädler, K.-H., & Kemel, K. 2012b, A&A, 539, A35
Brandenburg, A., Gressel, O., Käpylä, P. J., Kleeorin, N., Mantere, M. J., Rogachevskii, I. 2013, ApJ, 762, in press, arXiv:1211.2962
Elperin, T., Golubev I., Kleeorin, N., Rogachevskii, I. 2005, Phys. Rev. E, 71, 036302
Ji, H. 1999, Phys. Rev. Lett., 83, 3198
Käpylä, P. J., Brandenburg, A., Kleeorin, N., Mantere, M. J., & Rogachevskii, I. 2012, MNRAS, 422, 2465
Käpylä, P. J., Brandenburg, A., Kleeorin, N., Mantere, M. J., & Rogachevskii, I. 2013, Proceedings IAU Symposium No. 294 ”Solar and Astrophysical Dynamos and Magnetic Activity, Eds. A.G. Kosovichev, E.M. de Gouveia Dal Pino & Y. Yan, in press, arXiv:1211.2962
Kemel, K., Brandenburg, A., Kleeorin, N., Mitra, D., & Rogachevskii, I. 2012a, Solar Phys., arXiv:1203.1232, DOI:10.1007/s11207-012-0031-8
Kemel, K., Brandenburg, A., Kleeorin, N., & Rogachevskii, I. 2012b, Astron. Nachr., 333, 95
Kleeorin, N., Rogachevskii, I. 1994, Phys. Rev. E, 50, 2716
Kleeorin, N., Rogachevskii, I. 1999, Phys. Rev. E, 59, 6724
Kleeorin, N., Mond, M., Rogachevskii, I. 1993, Phys. Fluids B, 5, 4128
Kleeorin, N., Mond, M., Rogachevskii, I. 1996, A&A, 307, 293
Kleeorin, N.I., Rogachevskii, I.V., Ruzmaikin, A.A. 1989, Sov. Astron. Lett., 15, 274
Kleeorin, N.I., Rogachevskii, I.V., Ruzmaikin, A.A. 1990, Sov. Phys. JETP, 70, 878
Krause, F., & Rädler, K.-H. 1980, Mean-field magnetohydrodynamics and dynamo theory (Pergamon Press, Oxford)
Losada, I. R., Brandenburg, A., Kleeorin, N., Mitra, D., & Rogachevskii, I. 2012, A&A, 548, A49 (LBKMR)
Matthaeus, W. H., Goldstein, M. L., & Smith, C. 1982, Phys. Rev. Lett., 48, 1256
Moffatt, H.K. 1978, Magnetic field generation in electrically conducting fluids (Cambridge University Press, Cambridge)
Orszag, S. A. 1970, J. Fluid Mech., 41, 363
Ossendrijver, M. 2003, A&A Rev., 11, 287
Pouquet, A., Frisch, U., & Léorat, J. 1976, J. Fluid Mech., 77, 321
Parker, E.N. 1979, Cosmical magnetic fields (Oxford University Press, New York)
Rädler, K.-H., Kleeorin, N., & Rogachevskii, I. 2003, Geophys. Astrophys. Fluid Dyn., 97, 249
Roberts, P. H., & Soward, A. M. 1975, Astron. Nachr., 296, 49
Rogachevskii, I., & Kleeorin, N. 2004, Phys. Rev. E, 70, 046310
Rogachevskii, I., Kleeorin, N. 2007, Phys. Rev. E, 76, 056307
Rogachevskii, I., Kleeorin, N., Käpylä, P. J., Brandenburg, A., 2011, Phys. Rev. E, 84, 056314
Seehafer, N. 1996, Phys. Rev. E, 53, 1283
Steenbeck, M., Krause, F., & Rädler, K.-H. 1966, Z. Naturforsch., 21a, 369
Warnecke, J., Brandenburg, A., & Mitra, D. 2011, A&A, 534, A11
Warnecke, J., Brandenburg, A., & Mitra, D. 2012, J. Spa. Weather Spa. Clim., 2, A11
Zeldovich, Ya. B., Ruzmaikin, A. A., Sokoloff, D. D. 1983, Magnetic fields in astrophysics (Gordon & Breach, New York)
Zeldovich, Ya. B., Ruzmaikin, A. A., Sokoloff, D. D. 1990, The Almighty Chance (Word Scientific Publ, Singapore)

`$Header: /var/cvs/brandenb/tex/illa/DNS_rotation/paper.tex,v 1.5`